Research Article Vol. 59, No. 26 / 10 September 2020 / Applied Optics 7883

applied optics

Design of a superresolution large-aperture telescopic optical system with a wide field of view

Chao Wang,[1,2] Hao-dong Shi,[1,*] Zhuang Liu,[1] Qiang Fu,[1] Su Zhang,[1] Jun-tong Zhan,[1] Ying-chao Li,[1] Lun Jiang,[1] and Peng Zhang[1]

[1]School of Optoelectronic Engineering, Changchun University of Science and Technology, Changchun 130022, China
[2]State Key Laboratory of Applied Optics, Changchun Institute of Optics, Fine Mechanics and Physics, Chinese Academy of Sciences, Changchun 130022, China
*Corresponding author: jhl20092014@163.com

Received 27 April 2020; revised 7 July 2020; accepted 31 July 2020; posted 4 August 2020 (Doc. ID 396107); published 8 September 2020

A pupil modulator is a useful tool to improve the resolution of an optical imaging system beyond the classical diffraction limit. However, when this technology is used in a large-aperture telescopic imaging system, the field of view (FOV) with good superresolution (SR) imaging quality is significantly smaller than the designed FOV of the baseline optical system. In this paper, we investigate the influence of various aberrations on the SR properties of a telescopic system using a low sidelobe five-ring pure phase pupil modulator. On this basis, we propose an optimal design method for a wide FOV and a large-aperture telescopic baseline optical system with uniform image quality and a particular residue of symmetric aberration. The design results show that when the optimized 4 m aperture baseline optical system and the modulator are combined as the imaging system, the imaging system has a round and very similar point spread function in the FOV range of 0.28°; the SR gain ratio is 1.234–1.254; and the highest sidelobe intensity is less than 0.1; thus, the system maintains a high resolution ratio and a low sidelobe energy throughout the entire FOV. Finally, a reasonable tolerance model of the baseline optical system is established. The central symmetry tolerances are observed to be loose in this model, thereby reducing the cost and manufacturing difficulty of the system.

https://doi.org/10.1364/AO.396107

1. INTRODUCTION

The spatial frequency cutoff, or the optical resolution of an optical system, is strictly limited by the Rayleigh criterion $1.22\lambda/D$, where D is the optical pupil diameter and λ is the operating wavelength [1,2]. Therefore, the primary method used to enhance the resolution of a large-aperture telescopic imaging system in the past was to increase the optical aperture diameter, which induces an increase in the volume and weight of the system in a square ratio. In addition, the state-of-the-art limit of the large-aperture optics manufacturing has prompted the investigation of new methods to improve the optical resolution without changing the aperture of the optics, such as the pupil modulation (PM) technology. Its principle is to modulate the wavefront at the optical system pupil, making the core of the point spread function (PSF) narrower to improve the resolution [3,4]. PM superresolution (SR) technology was first used in microscopes [5,6], and it has gradually been applied to telescopes and antennas in recent years. For example, Cagigal and Canales first discussed the basic design techniques for SR PM that uses either variable transmittance pupils or phase masks for optical telescopes [7,8]. Vidal *et al.* discussed the effect of the adaptive technology on PM SR imaging results in the telescopic system [9]. Olmi *et al.* presented a feasible method to design antennas and telescopes with SR, which used variable transmittance pupils [10]. Luo discussed the sub-diffraction resolution of a telescope with a superoscillating element placed in the pupil plane [11]. Wang *et al.* presented the first proof-of-principle laboratory results of an SR lens-collimator optical system, mimicking a telescope configuration, employing a binary phase plate in the pupil plane [12].

When the existing PM SR technology is used in large-diameter telescopic systems, the field of view (FOV) with good SR imaging performance is significantly smaller than the FOV that can be achieved by the large-diameter baseline optical system. This is primarily owing to two reasons: (1) PM results in the decrease of the PSF mainlobe energy and the increase of the sidelobe energy. For a large sidelobe peak to mainlobe peak ratio, the mainlobe of an object point will be confused with the sidelobe of its adjacent object points in the imaging plane, resulting in blurred imaging. (2) The image quality of the telescopic optical baseline system in the full FOV is not uniform, and there is some asymmetric aberration left in the non-zero FOV. The imaging quality of this system may be good when the system is used in traditional imaging. However, when

the system is used in a SR far-field imaging, the tolerance of SR imaging to the asymmetric aberration is very tight. Thus, even though that although the field angle is significantly smaller than the maximum FOV of the baseline optical system, the SR effect of the focal light spot has been destroyed by the aberration. For reason (1), there are two types of solutions. The first solution employs the confocal scanning to suppress the sidelobe [13,14]; however, the disadvantage of using this solution is that real-time imaging in a large FOV cannot be realized. The second solution optimizes the modulation element structure to reduce the sidelobe energy. Liu *et al.* presented theories used to design a diffractive hybrid-type pupil filter with the highest sidelobe suppressed (highest sidelobe intensity <0.1) [15]. Xie *et al.* reported an optical SR imaging method based on a hybrid phase superoscillation pupil element with a high sidelobe suppression ratio (highest sidelobe intensity <0.2) [16]. Olmi *et al.* designed a complex transmittance pupil filter, which can achieve the desired trade-off between the width of the mainlobe and the level of the sidelobes [17]. According to Olmi's study, the sidelobe height and the mainlobe width are mutually restricted; therefore, the PSF sidelobe of SR systems must be higher than that of the Airy spot. When the sidelobe height of the PSF is less than 0.1, the SR system fulfills the imaging conditions in a wide FOV. For reason (2), little attention has been paid to it so far, and there is almost no prior literature on the design method of special baseline optical system for the SR telescopic imaging system.

In fact, for an SR imaging system, its pupil modulator and optical baseline system are combined, and the influence of different aberrations, introduced by the optical system, on the SR imaging result are not the same. If the baseline optical system is redesigned and optimized according to the characteristics of the SR imaging system, a real-time SR imaging system with a wide FOV may be obtained with the simplest structure, and the requirements for processing and adjustment accuracy will be relaxed, which will significantly promote the application of SR detection and imaging for long-distance targets, such as astronomy observation, optical surveillance, and remote sensing.

In this paper, a large-aperture SR telescopic imaging system with a relatively large FOV is designed. For the five-ring pure phase pupil filter, the influence of different types of aberrations on the SR performance is investigated, and the tolerance of each type of aberration is determined. On this basis, the optimal design of a telescopic optical system with uniform image quality and a spherical aberration remaining in the whole FOV is presented, and is proved to be of good SR performance in a wide FOV. Finally, the inverse limit sensitivity analysis for the system tolerance is conducted, which indicates that the system has a loose symmetric tolerance.

2. ANALYSIS OF EFFECTS OF DIFFERENT ABERRATIONS ON THE SR PROPERTIES

According to the diffraction theory [18], the normalized field measured at the observation plane in monochromatic light is given by

$$U(v,u)=2\int_0^1 P(\rho)\exp\left(-\frac{1}{2}iu\rho^2\right)J_0(v\rho)\rho\mathrm{d}\rho, \quad (1)$$

where ρ is the pupil normalized radial coordinate for the pupil, $P(\rho)$ is the pupil function, $J_0(\cdot)$ is the first kind zero-order Bessel function, and v and u are proportional to the axial and radial coordinates, respectively.

The SR properties of a pupil modulation imaging system can be determined by the following parameters: gain ratio G, highest sidelobe intensity M, and Strehl ratio S. Where G is defined as the ratio of the mainlobe radius of the Airy disk to the mainlobe radius of the superresolved pattern, M is the superresolved highest sidelobe intensity normalized by the mainlobe intensity of the superresolved pattern, and S is the Strehl ratio of the SR system. When $G > 1$, the limit resolution is improved; when $M < 0.1$, the mainlobe and sidelobe of adjacent points are less likely to be confused with each other on the imaging plane. Therefore, the system can achieve an improved imaging effect in the whole image plane.

In order to reduce the processing cost of the diffractive element, the pupil modulator in the paper is designed as a pure phase-only element of only 0 or π phase shift. For an operating wavelength of 632.8 nm and an optical system $F/\#$ of 12, the system focal plane light intensity has a suitable SR distribution when the modulator is a five-ring pure phase filter; the normalized radii of the five zones are 0.211, 0.36, 0.61, 0.7, and 1, as shown in Fig. 1 displays the system PSFs, before and after this phase modulator is added. For an ideal optical system, G is 1.27, M is 0.08, and $S = 0.307$.

It is well known that the Zernike polynomials represent a complete description of the aberrations of any imaging optical system with a circular pupil, and some aberration components are related to particular Zernike terms [19,20]. The first 16 terms of the Zernike Fringe polynomials represent the third-order to fifth-order aberrations, which can comprehensively represent the imaging quality of a large-aperture optical system [21].

Because the wavelength bandwidth of the diffraction element is very narrow, there is minimal chromatic aberration in the SR optical system. The SR system is primarily affected by the defocus, coma, astigmatism, and spherical aberration. Because the optical system is rotationally symmetric, a complete influence model can be established by studying the influence of Z_4 (defocus), Z_5 (third-order astigmatism), Z_7 (third-order coma), Z_9 (third-order spherical aberration), Z_{10} (trefoil), Z_{12} (fifth-order astigmatism), Z_{14} (fifth-order coma), and Z_{16} (fifth-order spherical aberration) on G, M, and S.

In the case of the optical wavefront with aberrations, the normalized distribution of complex amplitudes near the focus can be expressed as follows:

$$U(v,u)=2\int_0^1\int_0^{2\pi} P(\rho)\exp[\mathrm{i}\varphi(\rho,\theta)] \times\exp\left(-\frac{1}{2}\mathrm{i}u\rho^2\right)J_0(v\rho)\rho\mathrm{d}\rho\mathrm{d}\theta. \quad (2)$$

As shown in Fig. 2, the pupil function $P(\rho)$ in Eq. (2) can be expressed as

$$\begin{cases} P(\rho)=e^{0} & (0\le\rho<0.211,\ 0.36\le\rho<0.61,\ 0.7\le\rho\le1)\\ P(\rho)=e^{i\cdot\pi} & (0.211\le\rho<0.36,\ 0.61\le\rho<0.7)\end{cases}. \quad (3)$$

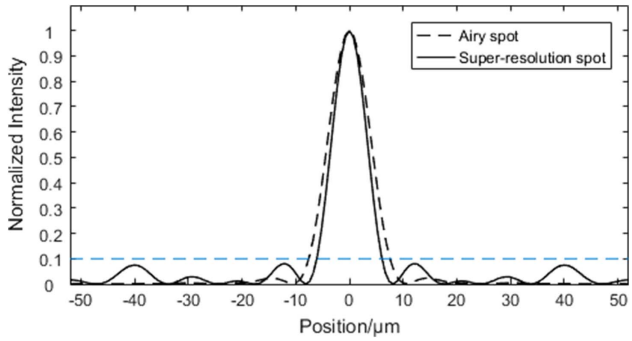

Fig. 1. Comparison of PSF before and after adding the phase modulator.

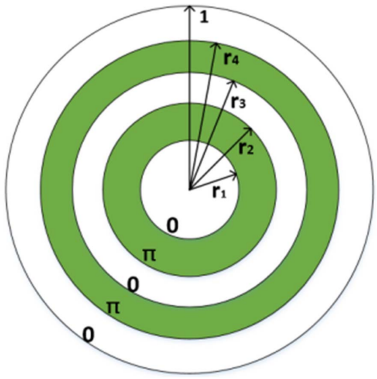

Fig. 2. Schematic diagram of the phase plate annular zone distribution.

The Zernike pupil function $\varphi(\rho, \theta)$ in Eq. (2) can be expressed as [22,23]

$$\varphi(\rho, \theta) = K \sum_{i=1}^{N} 2\pi \cdot A_i Z_i(\rho, \theta), \tag{4}$$

where θ is the angular ray coordinate, K is the diffraction order, N is the number of Zernike coefficients in the series, and A_i is the coefficient on the ith Zernike Fringe polynomial. The coefficients A_i all have units of waves.

In the following subsections, different types of aberrations are separately added to the pupil and the five-ring phase modulator that was designed previously is added to the system. To investigate the applicability of the SR imaging system to different types of aberrations and guide the design of the optical system, the influences of different types of wavefront aberrations on G, M, and S are recorded.

A. Defocus

The effect of defocus (Z_4) on SR imaging with the five-ring phase modulator is shown in Fig. 3.

It can be observed from Fig. 3 that G first increases and then decreases with the magnitude of defocus, indicating that the moderate defocus can enhance the SR power. When defocus reaches approximately 0.28 λ, G is at its maximum, exceeding

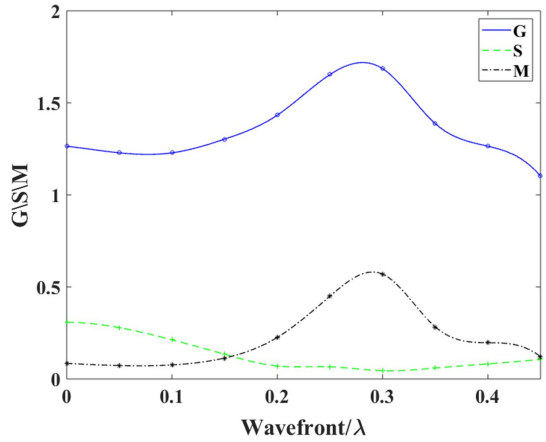

Fig. 3. G, S, and M varying with the effects of defocus.

1.7; however, M has also increased to 0.6 and S decreases to approximately 0.1. It is clear that stray light with high energy will be introduced by the sidelobe. For SR imaging in a large FOV, we set that G is no less than 1.2, S is no less than 0.15, and M is no more than 0.1 as the evaluation criteria for good imaging. Using this standard, according to the results of Fig. 3, the defocus should be controlled below 0.15 λ in the actual optical system design.

B. Astigmatism

The pupils with third-order astigmatism (Z_5), trefoil (Z_{10}), and fifth-order astigmatism (Z_{12}) are modulated by the five-ring phase plate respectively. The corresponding optical system PSFs are shown in Figs. 4–6, respectively.

It can be observed from Figs. 4–6 that for the aberrations induced by third-order astigmatism, trefoil, and fifth-order astigmatism, G changes slowly with an increase in the astigmatism amplitude; however, the sidelobe factor M increases rapidly. When any of these aberration exceeds 0.07 λ, the M value in one of the x- or y-directions will definitely be greater than 0.1. Therefore, the astigmatism should be strictly controlled in the design of a baseline optical system.

C. Coma

The effect of third-order coma (Z_7) and fifth-order coma (Z_{14}) on SR imaging is shown in Figs. 7 and 8.

It can be observed from Figs. 7 and 8 that for both low- and high-order coma, a coma value greater than 0.06 λ results in an M value greater than 0.1 in one of the x- and y-directions. Furthermore, by comparing the PSFs in the x- and y-directions of the system, with added fifth-order coma, it can be observed that the coma will reduce the rotational symmetry of the PSF. Therefore, the coma should be strictly controlled in the design of the baseline optical system.

D. Spherical Aberration

The effect of the third-order spherical aberration (Z_9) and fifth-order spherical aberration (Z_{16}) on SR imaging is shown in Fig. 9.

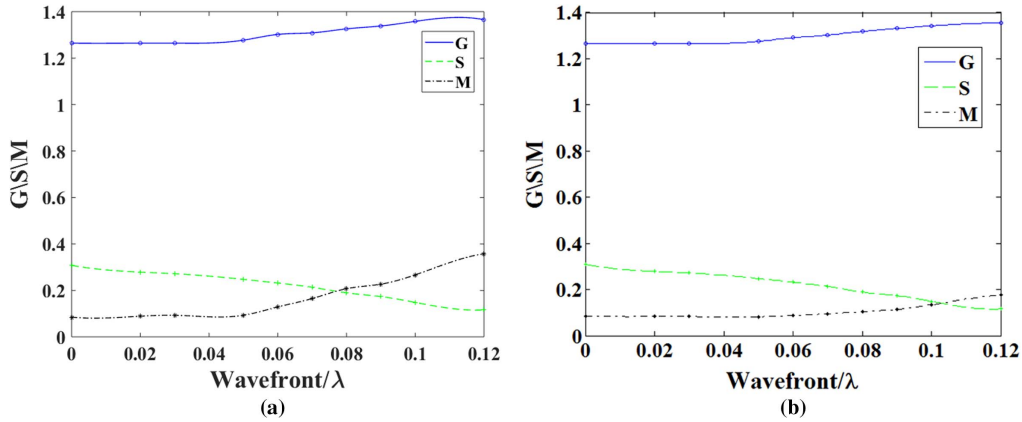

Fig. 4. Variation of G, S, and M with third-order astigmatism in the (a) x-direction and (b) y-direction.

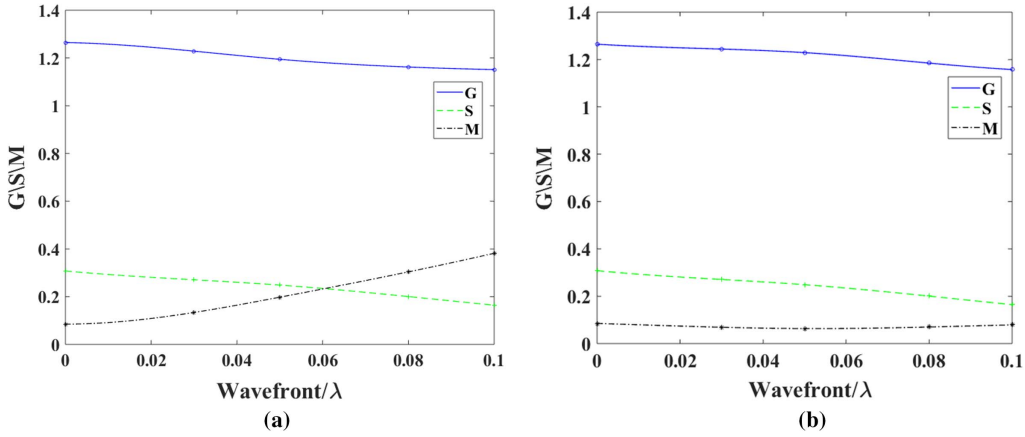

Fig. 5. Variation of G, S, and M with trefoil in the (a) x-direction and (b) y-direction.

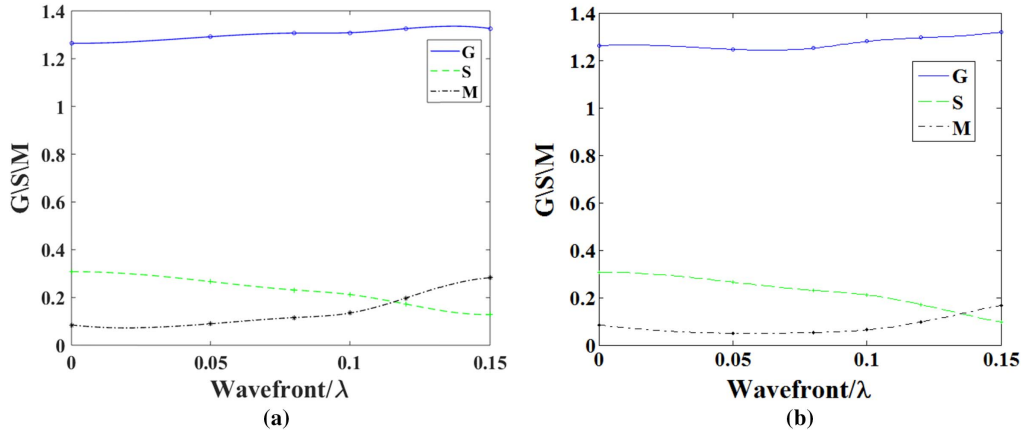

Fig. 6. Variation of G, S, and M with fifth-order astigmatism in the (a) x-direction and (b) y-direction.

It can be observed that the system possesses good SR imaging quality when the third-order or fifth-order spherical aberration is less than 0.1 λ. The sidelobe energy increases slightly with an increase of the spherical aberration; however, before the wavefront error root mean square (RMS) reaches to 0.2 λ, M is basically stable at approximately 0.1. It can be seen that the SR imaging system has a high tolerance for spherical aberration, which will not induce a significant increase in sidelobe energy. Additionally, the spherical aberration will not destroy the symmetry of the focal spot.

We consider the condition of defocus and the spherical aberration simultaneously existing in the pupil. Because the middle part of the wavefront fluctuations caused by defocus and spherical aberration of different symbols is in the opposite direction, the two aberrations can compensate each other, which flattens the wavefront in the pupil plane. For the SR modulator

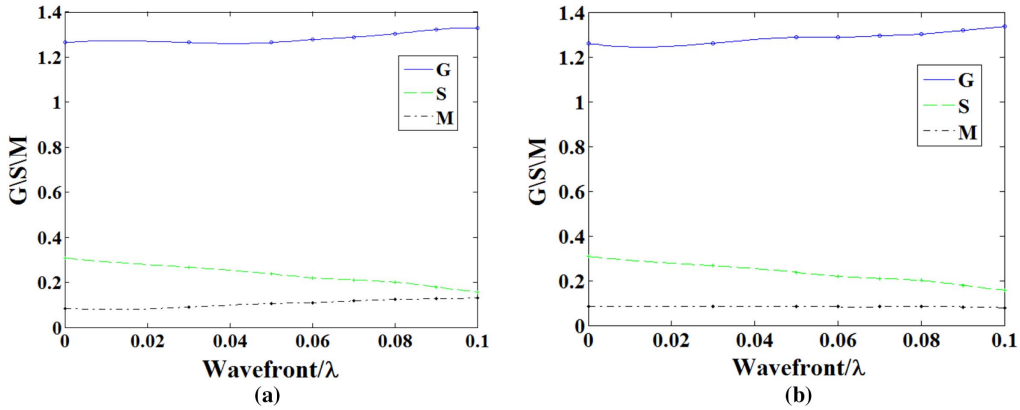

Fig. 7. Variation of G, S, and M with third-order coma in the (a) x-direction and (b) y-direction.

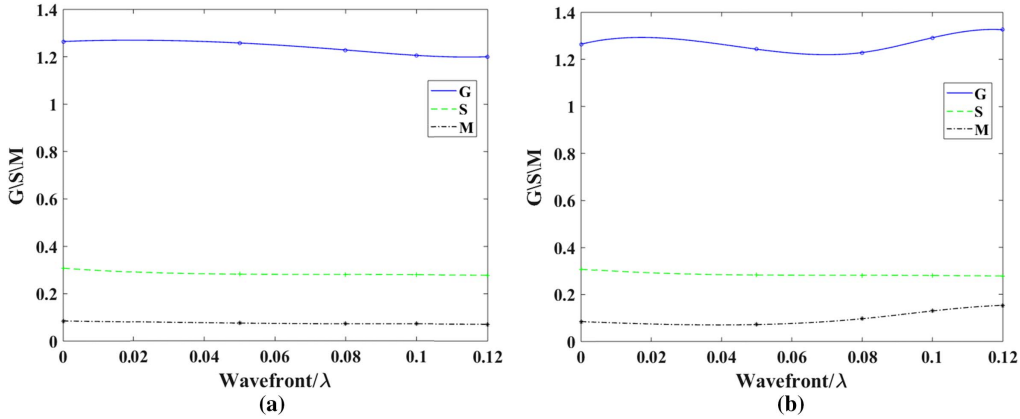

Fig. 8. Variation of G, S, and M with fifth-order coma in the (a) x-direction and (b) y-direction.

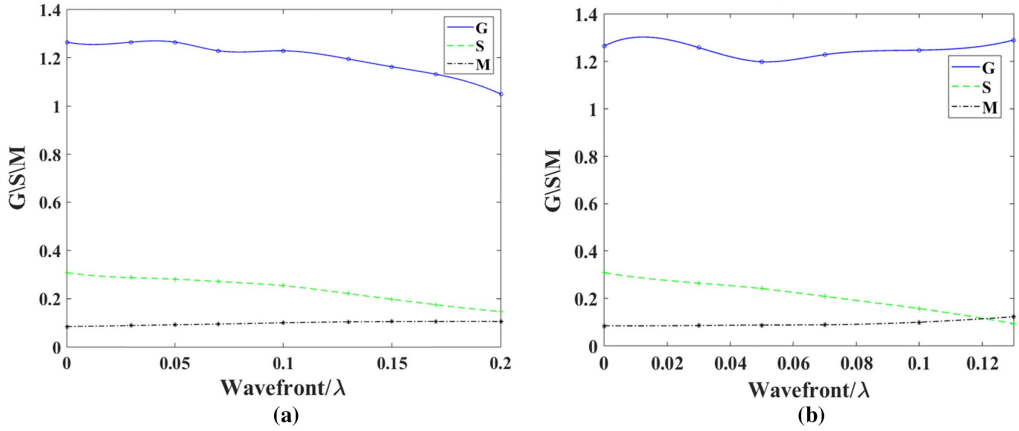

Fig. 9. Variation of G, S, and M with (a) third-order spherical aberration and (b) fifth-order spherical aberration.

in this study, a third-order spherical aberration of 0.2 λ induces a decrease in G to 1.038 and an increase to M to 0.25. For a defocus of 0.355 λ further added to the pupil, the mainlobe diameter decreased from 17.8 μm to 14.582 μm, G increased to 1.27, and M decreased to 0.083, as shown in Fig. 10. Although the defocus and spherical aberration have exceeded the tolerance limit above, they can compensate each other, which can not only improve the resolution of the system, but also reduce the sidelobe peak energy. In summary, in order to improve the performance of SR imaging and ensure that different image points do not interfere with each other, the astigmatism and coma should be effectively suppressed. The spherical aberration and defocus can be retained as appropriate and their amplitudes should be precisely optimized.

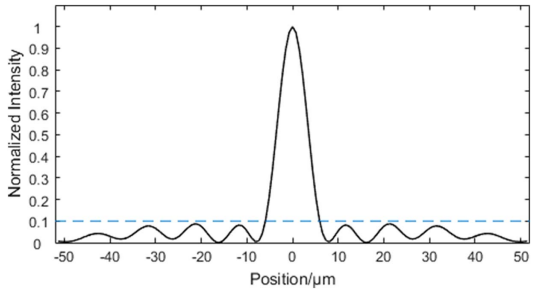

Fig. 10. SR imaging PSF with simultaneous 0.2 λ spherical aberration and −0.355 λ defocus.

3. OPTIMAL DESIGN METHOD OF THE OPTICAL SYSTEM

In this study, an optical system for the SR imaging is designed. The parameters of the optical system are $F\# = 12$, focal length = 48 m, FOV = 0.28°, and operating wavelength between 623 and 643 nm. The optical system without a phase modulator, which is defined as the baseline optical system, is composed of a telescope unit and a relay imaging unit. Because the optical pupil diameter of this system is large, the telescope unit is in the form of a Cassegrain telescope, which produces a primary image surface, where the anti-stray stop can be placed. The relay imaging unit is a lens group. The pupil filter element requires that the incident beam should be perpendicular to the element surface; thus, the diverging beam from the Cassegrain unit is first collimated, and subsequently converged by the relay imaging optics. The converging spot is received by the detector. The SR phase plate designed above is placed in the collimated beam, and the position of the plate is the intermediate pupil of the optical system.

To improve the SR imaging effect in a wide field of view, there are special requirements for the baseline optical system: there should be measures in place to control the chromatic aberration; the non-rotational symmetry items, such as the coma and astigmatism, should be corrected in the entire FOV; and the spot diagram and aberration distributions at different FOV angles should be similar. To meet these requirements, the optimization operands AXCL and REAY are employed to suppress the axial and lateral chromatic aberration in the optical design with ZEMAX; the operand ZERN is used to limit the coma and astigmatism to 0 and to control the third- and fifth-order spherical aberrations below 0.2 λ and 0.1 λ, respectively. In addition, the ZEMAX programming language (ZPL) is used to write a user-defined merit function to achieve further optimization operation. It is simple to call the ZPL macro in the optical design process. The programming principle of this macro is as follows: the DENC operand is employed to evaluate the energy concentration of the PSF at any FOV and wavelength, which is achieved by computing the encircled radius of the diffraction energy. The smaller the radius, the higher the energy concentration and the better the imaging quality. Thus, the merit function can be expressed as

$$\text{Merit Function} = \sqrt{\frac{(\sum r_i)^2 + \sum w_i (r_i/r_0 - 1)^2}{1 + (\sum w_i)}}, \quad (5)$$

where r_0 is the encircled radius at the 0 field, r_i and w_i are the encircled radius and optimization weight at different FOV points, respectively. Optimization of Eq. (5) results in a similar and minimized encircled radius for different FOVs to improve the imaging quality. Because DENC can indirectly suppress defocus by controlling the energy encircled radius, we do not add an independent operand to control defocus in the optimization process. When the optical system has been designed according to the above method, and the pupil filter is added to the appropriate position in the system, the best SR imaging performance can be achieved by adjusting the image plane position (equivalent to fine tuning the defocus of the system).

4. RESULTS

A. Comparison of Design Results between the Traditional and Uniform Imaging Methods

First, the results of the optical system designed according to the traditional design method of minimizing the RMS spot radius of the system are presented [24,25]. The modulation transfer function (MTF) and spot diagram are shown Fig. 11. It can be seen that the RMS radius on the marginal FOV is close to that of the Airy spot, which fulfills the requirements of traditional imaging. However, after the phase modulator is added to the system, the PSF of the marginal FOV is significantly different from that of the center FOV, and the marginal FOV PSFs in some directions display no SR effect, as shown in Fig. 12. PSF data is obtained by the "FFT PSF Cross Section" option in ZEMAX. The amplitude of each aberration on the marginal FOV at 632.8 nm is presented in Table 1, in which the third-order coma is the primary factor leading to the deformation of the SR spot, which is consistent with the analysis in Section 2.

The results of the design method for the uniform image quality in the whole FOV are presented below. The final imaging system layout is shown in Fig. 13.

The final spot diagram of the baseline optical system is shown in Fig. 14. The wavefront error of the worst marginal FOV is approximately 1/5 λ RMS. Table 2 shows the Zernike aberration distribution of the marginal FOV at 632.8 nm. It can be observed from Fig. 14 that the residual spherical aberration is obvious at each FOV, but the spots in different FOVs are very similar. The Airy spot diameter of this system is 18.478 μm, and the SR PSF intensity distribution at each FOV after the phase modulator is added in the system is shown in Fig. 15. In polychromatic light with 20 nm spectral bandwidth, the value of G of the three fields is 1.234, 1.252, and 1.254; S is 0.303, 0.302, and 0.295; and M is 0.069, 0.075, and 0.088, respectively. This shows that the optimization method for uniform image quality in the design has achieved good results. The imaging quality of each FOV is similar, and the high SR factor and low sidelobe energy are maintained in the whole FOV. Figure 16 shows the imaging performance of the SR imaging system on the extended target for different FOVs. It can be observed that the imaging of the SR system for different FOVs is similar, and the details that cannot be resolved by the diffraction-limited optics [Fig. 16(a)] can be distinguished by this SR imaging system, including the eight points which compose "□" and the seven points of "F".

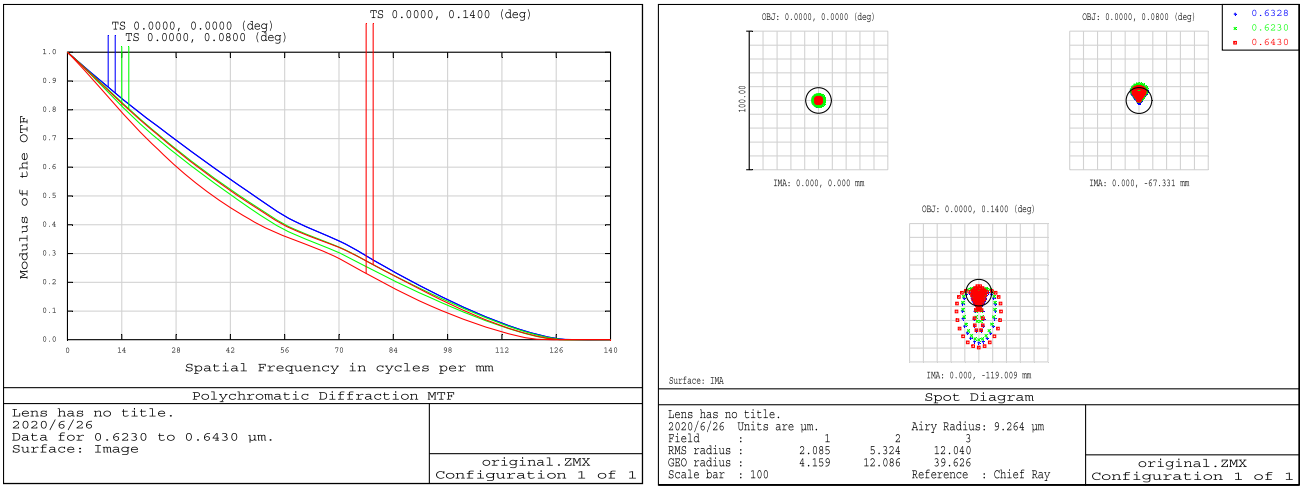

(a) (b)

Fig. 11. Image quality of the optical baseline system optimized by traditional methods: (a) MTF and (b) spot diagram.

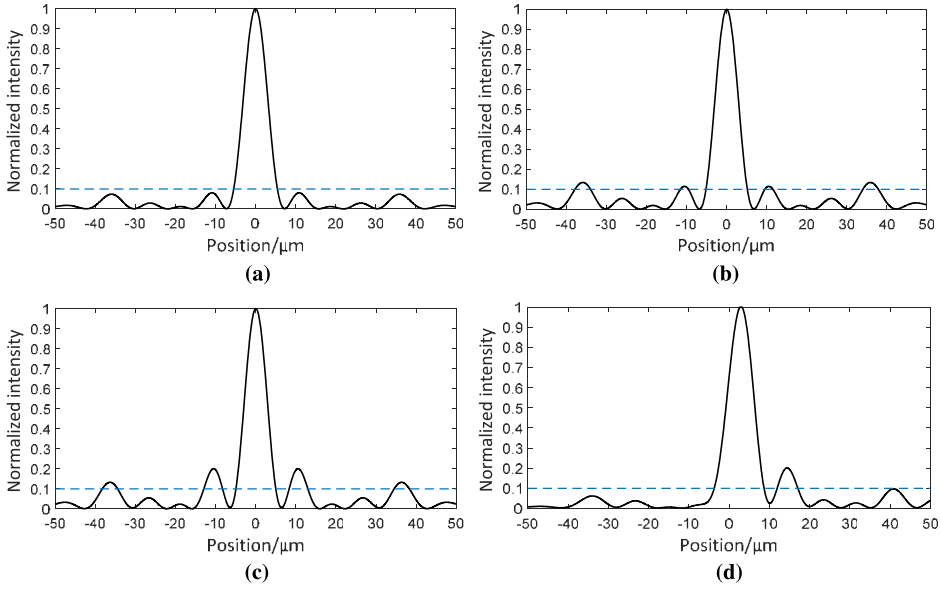

Fig. 12. PSFs of each FOV after the modulator added: (a) 0°, (b) 0.16°, (c) 0.28° (x-direction), and (d) 0.28° (y-direction).

Table 1. Marginal Field Aberration of the Optical Baseline System Optimized by Traditional Methods

Aberration	Defocus	3rd COMA	3rd ASTI	3rd SPHA	Trefiol	5th COMA	5th ASTI	5th SPHA
Value	−0.0802	0.1366	−0.0563	0.0255	0.0136	0.0103	−0.0066	−0.0007

Table 2. Marginal Field Aberration of the Optical Baseline System with Uniform Image Quality in the Whole Field

Aberration	Defocus	3rd COMA	3rd ASTI	3rd SPHA	Trefoil	5th COMA	5th ASTI	5th SPHA
Value	−0.1730	−0.0543	0.0321	−0.0778	0.0047	−0.0160	0.0048	−0.0444

The impact of environmental change on the SR imaging system is analyzed. The SR system design temperature is 20°C. The SR parameters at 5°C, 10°C, 15°C, 25°C, 30°C, and 35°C are simulated, and the results are shown in Table 3. The results show that in the range of 20 ± 15°C, there is minimal change in the value of G; the difference between the maximum and minimum values of S does not exceed 0.014; and the difference between the maximum and minimum values of M does not exceed 0.001. It can be observed that the requirements of the system for temperature control are relatively relaxed. This is

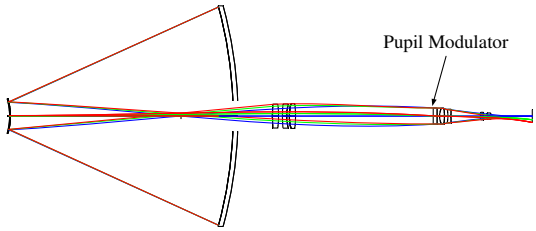

Fig. 13. SR telescopic imaging optical system designed by the novel method.

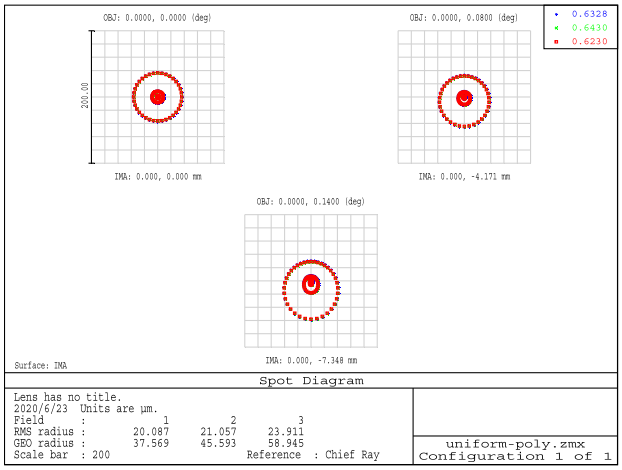

Fig. 14. Spot diagram in different FOVs.

Table 3. Range of *G*, *S*, and *M* within a Temperature Range of 5°C–35°C

	0	0.16°	0.28°
G	1.234–1.234	1.232–1.232	1.254–1.254
S	0.295–0.305	0.294–0.306	0.289–0.303
M	0.069–0.072	0.074–0.076	0.088–0.090

because the temperature change primarily causes defocus, which has a relatively small influence on this SR system according to Section 2.

B. Tolerance Model of Optical Baseline System with Uniform Image Quality

Different types of aberration have great significant influence on the SR imaging. Considering that the SR imaging system has a high tolerance for the spherical aberration and defocus, and these two types of aberration can also compensate each other, we relax the tolerance that will induce the rotational symmetry aberration, such as fringes (curvature radius) and thickness, etc. The tolerance which may cause asymmetric aberration, such as decenter and tilt, is more strictly maintained. The tolerance inverse limit sensitivity analysis is conducted by the optical design software. For the evaluation standard, the coefficients of the third- to fifth-order coma, astigmatism, or trefoil of the system should not exceed the tolerance limit stated in Section 2: the encircled radius at different FOVs is nearly equal and not

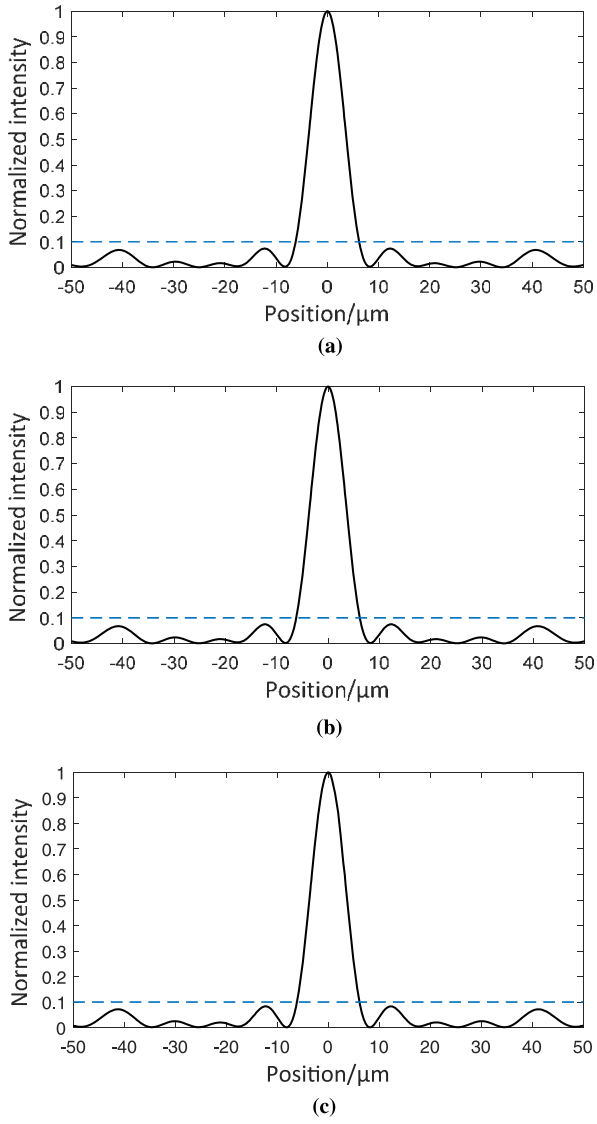

Fig. 15. Cross section of SR PSFs after added modulation of (a) 0°, (b) 0.16°, and (c) 0.28°.

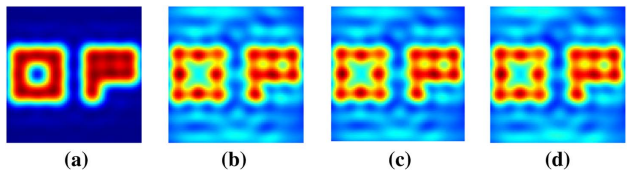

Fig. 16. Imaging simulations of the extended target on (a) the diffraction limit, (b) 0°, (c) 0.16°, and (d) 0.28°.

less than 15 µm or more than 25 µm; the difference between the *x*-direction radius and *y*-direction radius of the RMS spots at different FOVs is within 10%; and the radii of the RMS spots for different FOVs are not greater than 25 µm. The compensator is the system back focal length. Using the ZPL macro, the user-defined tolerance scripts are compiled and linked with the software. Tables 4 and 5 show the tolerance system for the optical system fabrication and alignment. As observed from

Table 4. Tolerances for Processing and Alignment of the Reflection Part of the System

Surface	Radius/mm	Conic	Interval/mm	Mirror Decenter/mm	Mirror Tilt/arc min
Primary mirror	±0.5	±0.0006	±0.04	±0.02	±0.2
Secondary mirror	±0.5	±0.005	—	±0.02	±0.2

Table 5. Tolerances for Processing and Alignment of the Transmission Part of the System

Lens	Fringes/ fringe	Surface Irregularity/fringe	Surface Tilts/ arc min	Thickness/mm	Index	Interval/mm	Element Decenter/mm	Element Tilts/arc min
Lens 1	±3	±0.2	±0.5	±0.1	±0.001	±0.1	±0.02	±0.3
Lens 2	±3	±0.2	±0.5	±0.1	±0.001	±0.1	±0.02	±0.3
Lens 3	±3	±0.2	±0.5	±0.1	±0.001	±0.1	±0.02	±0.3
Lens 4	±3	±0.2	±0.5	±0.1	±0.001	±0.1	±0.02	±0.3
Lens 5	±3	±0.2	±0.5	±0.04	±0.001	±0.1	±0.02	±0.3
Lens 6	±3	±0.2	±0.5	±0.1	±0.001	±0.1	±0.02	±0.3
Lens 7	±3	±0.2	±0.5	±0.1	±0.001	±0.1	±0.02	±0.3

Table 6. Least Favorable Values of *G*, *S*, and *M* in the Tolerance Analysis

	0	0.16°	0.28°
G	1.212	1.201	1.194
S	0.203	0.202	0.167
M	0.078	0.086	0.092

these tables, rotational symmetry tolerances such as the radius, conic, and interval of the mirrors, and the fringes, thickness, refractive index, and interval of the lens are relaxed; thus, greater allowance is reserved for the SR optical system manufacturing process. And the non-symmetry tolerances such as tilt, decenter, and surface irregularity can also be satisfied with the current machining and alignment accuracy. Five hundred random lenses are generated in the analysis, and we save each of them and analyze their respective SR parameters. Table 6 presents the least favorable values of G, S, and M for all random samples. In Table 6, $G \geq 1.2$ and $M < 0.1$, which shows that the system maintains a low-sidelobe SR effect throughout the entire FOV under the tolerance limit.

5. CONCLUSIONS

The effects of various types of aberrations, such as defocus, coma, astigmatism, and spherical aberration, on the properties of an SR imaging system with a low sidelobe factor five-ring pupil modulator are investigated. The tolerance of each aberration term is given, and it is identified out that in SR telescopic imaging systems, asymmetric aberration such as coma and astigmatism need to be strictly suppressed; however, symmetric aberrations have a minimal effect and may complement each other. Based on this analysis, a special optimization function is compiled to design a large-aperture telescope SR baseline optical system. For the design results, the SR gain ratio in the full FOV is 1.234–1.254, the Strehl ratio is 0.295–0.303, and the peak sidelobe intensity is 0.069–0.088. The result has very similar PSFs in the FOV range of 0.28° and maintains a sub-diffraction resolution and low sidelobe energy. The tolerance model of the system is established, and it is found that the system has a large margin on the central symmetry tolerance, which reduces the cost and difficulty of machining and assembly. Because the Strehl ratio of this system is relatively low, a variable pupil modulator can be used in the practical application. For weak observation targets, the pupil is not modulated to obtain a high Strehl ratio. For bright targets, the phase modulator in this study is used to obtain a high angular resolution. In future work, we will improve the optical structure to further expand the FOV, and attempt other types of modulators to widen the operating spectral range of the system. In addition, because parameters of a phase modulator can be optimized by mathematical software programs, in the next step we will use the dynamic data exchange method to share data between the optical software and the calculation program, to simultaneously optimize the baseline optical system and the modulator to obtain improved design results.

Funding. National Natural Science Foundation of China (61701045, 61705019, 61805027, 61805028, 61890960); Joint Fund of Astronomy (U1731240); special fund of DSTI (KJSP2016010202); Education Department of Jilin Province (JJKH20190563KJ); the Natural Science Foundation of Jilin (20180101338JC); Open fund of State Key Laboratory of Applied Optics (SKLAO2020001A11); Open fund of Key Laboratory of Airborne Optical Imaging and Measurement, Chinese Academy of Sciences (No. HCKF-201912GX01).

Disclosures. The authors declare no conflicts of interest.

REFERENCES

1. E. Abbé, "Beiträge zur theorie des mikroskops under mikroskopischen wahrnehmung," Archiv. Mickrosk. Anat. **9**, 413–418 (1873).
2. J. Jia, C. Zhou, and L. Liu, "Superresolution technology for reduction of the far-field diffraction spot size in the laser free-space communication system," Opt. Commun. **228**, 271–278 (2003).
3. I. J. Cox, C. J. R. Sheppard, and T. Wilson, "Reappraisal of arrays of concentric annuli as super resolving filters," J. Opt. Soc. Am. **72**, 1287–1291 (1982).

4. T. R. M. Sales and G. M. Morris, "Diffractive super resolution elements," J. Opt. Soc. Am. A **14**, 1637–1646 (1997).
5. M. R. Rai, A. Vijayakumar, and J. Rosen, "Super resolution beyond the diffraction limit using phase spatial light modulator between incoherently illuminated objects and the entrance of an imaging system," Opt. Lett. **44**, 1572–1575 (2019).
6. E. Ronzitti, G. Vicidomini, V. Caorsi, and A. Diaspro, "Annular pupil filter under shot-noise condition for linear and nonlinear microscopy," Opt. Express **17**, 6867–6879 (2009).
7. M. P. Cagigal, V. F. Canales, and J. E. Oti, "Design of continuous superresolving masks for ground-based telescopes," Publ. Astron. Soc. Pac. **116**, 965–970 (2004).
8. M. A. A. Neil, R. Juskaitis, T. Wilson, Z. J. Laczik, and V. Sarafis, "Optimized pupil-plane filters for confocal microscope point-spread function engineering," Opt. Lett. **25**, 245–247 (2000).
9. V. F. Canales, D. M. Juana, and M. P. Cagigal, "Super resolution in compensated telescopes," Opt. Lett. **29**, 935–937 (2004).
10. L. Olmi, P. Bolli, L. Cresci, F. D'Agostino, M. Migliozzi, D. Mugnai, E. Natale, R. Nesti, D. Panella, and L. Stefani, "Laboratory measurements of super-resolving Toraldo pupils for radio astronomical applications," Exp. Astron. **43**, 285–309 (2017).
11. X. Luo, "Sub-diffraction-limited telescopies," in *Engineering Optics 2.0* (Springer, 2019), Chap. 8.
12. C. T. Wang, D. L. Tang, Y. Q. Wang, Z. Y. Zhao, J. Wang, M. B. Pu, Y. D. Zhang, W. Yan, P. Gao, and X. G. Luo, "Super-resolution optical telescopes with local light diffraction shrinkage," Sci. Rep. **5**, 18485 (2015).
13. N. Wei, "Investigation of far-field super-resolution imaging method based on super-oscillatory phenomenon," Ph.D. dissertation (University of Chinese Academy of Sciences, 2016), Chap. 3, 1–105.
14. W. Zha, J. Chang, W. Chen, H. Yang, and X. Yan, "Tolerance analysis of a super-resolution optical system," Proc. SPIE **9298**, 92981V (2014).
15. H. T. Liu, Y. B. Yan, and G. F. Jin, "Design theories and performance limits of diffractive superresolution elements with the highest sidelobe suppressed," J. Opt. Soc. Am. A **22**, 828–838 (2005).
16. Q. K. Xie, Y. R. Jiang, J. Liang, A. L. Ren, and E. Qu, "Hybrid phase-amplitude superoscillation element for nonscanning optical superresolution imaging," J. Opt. Soc. Am. A **36**, 196–201 (2019).
17. L. Olmi, P. Bolli, L. Carbonaro, L. Cresci, D. Mugnai, E. Natale, R. Nesti, D. Panella, R. Juri, and Z. Giampaolo, "Design of super-resolving Toraldo Pupils for radio astronomical applications," *32nd General Assembly and Scientific Symposium of the International Union of Radio Science (URSI GASS)*, Montreal, Quebec, Canada, 2017, pp. 1–4.
18. M. Born and E. Wolf, *Principles of Optics* (Cambridge University, 1999), pp. 484–494.
19. R. K. Tyson, "Conversion of Zernike aberration coefficients to seidel and higher-order power-series aberration coefficients," Opt. Lett. **7**, 262–264 (1982).
20. V. N. Mahajan, "Zernike-Gauss polynomials and optical aberrations of systems with Gaussian pupils," Appl. Opt. **34**, 8057–8059 (1995).
21. R. W. Gray, C. Dunn, K. P. Thompson, and J. P. Rolland, "An analytic expression for the field dependence of Zernike polynomials in rotationally symmetric optical systems," Opt. Express **20**, 16436–16449 (2012).
22. X. Hou, F. Wu, L. Yang, and S. Wu, "Full-aperture wavefront reconstruction from annular subaperture interferometric data by use of Zernike annular polynomials and a matrix method for testing large aspheric surfaces," Appl. Opt. **45**, 3443–3455 (2016).
23. R. J. Noll, "Zernike polynomials and atmospheric turbulence," J. Opt. Soc. Am. **66**, 207–211 (1976).
24. E. Atad-Ettedgui and S. P. Worswick, "Optical design concept of the 4-m visible and infrared survey telescope for astronomy," Proc. SPIE **4842**, 95–105 (2003).
25. A. Swat, D. O'Donoghue, J. Swiegers, L. Nel, and D. A. H. Buckley, "The optical design of the Southern African Large Telescope (SALT)," Proc. SPIE **4837**, 564–575 (2003).